Nano Research

Open Access

Research Article

Controllable photooxidation of 1-phenylethanol integrated with hydrogen evolution by a polyoxometalate/$ZnIn_2S_4$/WO_3 catalytic system

Jiaxin Yang[1,2], Yongkang Liu[2], Yun Qin[2], Zhenheng Diao[1]✉, Yuanyuan Dong[2]✉, and Hongjin Lv[2]✉

[1] *School of Chemical Engineering, Advanced Institute of Materials Science, Changchun University of Technology, Changchun 130012, China*
[2] *MOE Key Laboratory of Cluster Science, Beijing Key Laboratory of Photoelectric/Electrophotonic Conversion Materials, School of Chemistry and Chemical Engineering, Beijing Institute of Technology, Beijing 102488, China*

Cite this article: *Nano Research*, **2025**, *18*, 94907303. https://doi.org/10.26599/NR.2025.94907303

ABSTRACT: The photocatalytic oxidation of 1-phenylethanol coupling with hydrogen evolution represents a promising strategy for the full utilization of the photogenerated electrons and holes to accomplish the maximum conversion of solar energy into chemical energy. To date, however, the controllable of reaction path and product distribution has yet not to be unrevealed. Herein, we report an efficient coupled catalytic system composed of $ZnIn_2S_4$/WO_3 S-scheme heterojunction and Ni-containing polyoxometalate ($[Ni_4(H_2O)_2(PW_9O_{34})_2]^{10-}$ (**Ni_4P_2**)), which exhibited excellent photocatalytic activities towards the oxidation valorization of 1-phenylethanol coupling with hydrogen evolution. The addition of **Ni_4P_2** can efficiently control the product distribution. Specifically, 1-phenylethanol was preferentially converted to pinacol (86.0% selectivity) via C–C coupling over $ZnIn_2S_4$/WO_3 S-scheme heterojunction accompanied by hydrogen production (202.4 μmol), whereas it would be converted to acetophenone (93.8% selectivity) by photogenerated holes with concomitant hydrogen formation (183.1 μmol) over the coupled **Ni_4P_2**/$ZnIn_2S_4$/WO_3 catalytic system. Mechanism studies revealed that the hydrogen evolution cocatalyst **Ni_4P_2**, with its excellent electron storage capacity, can compete with the oxidation product acetophenone for electrons, and thus its addition can significantly inhibit the reduction of acetophenone, resulting in the inability to generate the coupling product pinacol.

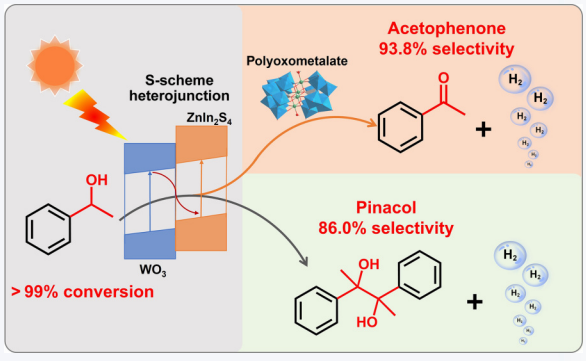

KEYWORDS: S-scheme heterojunction, $ZnIn_2S_4$, polyoxometalates, dehydrocoupling, hydrogen evolution, photocatalysis

1 Introduction

Hydrogen has been regarded as a promising energy vector due to its alternative to traditional fossil fuel, which can be widely applied in the field of fuel cell and the hydrogenation synthesis of renewable liquid fuel [1]. To date, H_2 is almost exclusively produced via the reforming/gasification of fossil-derived fuels (coal, gas, or oil), which is energy-intensive and unsustainable [2]. Solar-driven H_2 evolution via water splitting has therefore received substantial attention since the pioneering work of Fujishima and Honda [3]. Unfortunately, using the sacrificial electron donor as hole scavengers in this conventional strategy wastes the oxidizing power of the excited holes. It is a promising alternative strategy to designing the oxidation valorization of organic substrates coupling with hydrogen evolution to accomplish the full utilization of the photogenerated electrons and holes. 1-phenylethanol, a kind of biomass derivates, is a functional structural unit in the synthesis of various drug compounds [4]. Therefore, it is highly valuable to study the valorization transformation of 1-phenylethanol coupling with hydrogen production.

The separation efficiency of the photogenerated charge carriers is essential for the photocatalytic activities in photocatalysis process [5]. The construction of S-scheme heterojunction can facilitate the efficient charge carriers separation and maximize the redox capacity of the photocatalyst due to the reservation of the powerful photogenerated electrons and holes in conduction band (CB) of the reduction photocatalyst and valence band (VB) of the oxidation

Received: January 5, 2025; **Revised:** February 11, 2025
Accepted: February 12, 2025

✉Address correspondence to Zhenheng Diao, diaozhenheng@ccut.edu.cn; Yuanyuan Dong, dyy1111@bit.edu.cn; Hongjin Lv, hlv@bit.edu.cn

photocatalyst, respectively [6]. Several S-scheme heterojunctions, such as WO_3/g-C_3N_4 [7], Fe_2O_3/Bi_2MoO_6 [8], TiO_2@$ZnIn_2S_4$ [9], and BiOBr/NiO [10], have thus been fabricated and applied to hydrogen evolution [11], CO_2 reduction [12, 13], H_2O_2 production [14], and pollutant removal [15]. $ZnIn_2S_4$ exhibited the good catalytic activities in photocatalytic reduction processes such as hydrogen evolution and CO_2 reduction and thus be considered as a popular reduction photocatalyst [4, 16]. WO_3 is usually used as the oxidation photocatalyst due to the positive VB, low cost, and anti-corrosion [17, 18]. Additionally, two-dimensional (2D) S-scheme heterojunctions with the extensive specific surface areas exposed a flood of surface unsaturated atoms that functioned as active sites and reduced the frequency of the electron-hole recombination from the interior to surface, thus possessing the distinct advantages in terms of light harvesting, utilization, and reaction [6]. Therefore, 2D $ZnIn_2S_4$ nanosheets and WO_3 nanorods were selected to fabricate S-scheme heterojunction ($ZnIn_2S_4$/WO_3, denoted as **ZIS/WO$_3$**) and further applied to the photocatalytic oxidation valorization of 1-phenylethanol coupling with hydrogen production.

In the oxidation end of this photocatalytic process, the conversion of 1-phenylethanol follows the two paths: the conversion of 1-phenylethanol to acetophenone via oxidation reaction and the transformation of 1-phenylethanol into pinacol via C–C coupling reaction. However, the modulation of reaction path and product distribution has not yet been reported. Meanwhile, the activity of this photocatalytic reaction also depends on the hydrogen evolution reaction activity in the reduction end. Hydrogen evolution catalyst is thus included in the photocatalytic system of this work. Transition metal-containing polyoxometalates (POMs), especially for Ni-containing polyoxometalates, can efficiently catalyze hydrogen evolution [19]. A series of Ni-containing POMs were reported, such as $Na_6K_4[Ni_4(H_2O)_2(PW_9O_{34})_2]\cdot 32H_2O$ (Na_6K_4-**Ni_4P_2**) [20], $[\{Ni_4(OH)_3AsO_4\}_4(B\text{-}a\text{-}PW_9O_{34})_4]^{28-}$ (**$Ni_{16}As_4P_4$**) [21], $[Ni(H_2O)GeW_{11}O_{39}]^{6-}$ (**$NiGeW_{11}$**) [22], $[Ni_{16}(H_2O)_{15}(OH)_9(PO_4)_4(SiW_9O_{34})_3]^{19-}$ (**$Ni_{16}P_4(SiW_9)_3$**) [23], $(P_2NC_{36}H_{30})_8Na_4[(\alpha\text{-}A\text{-}SiW_9O_{34})Ni^{II}{}_{14}(AleOH)_5(AleO)_2(H_2O)_{11}(OH)_7]\cdot 60H_2O$ (**$Ni_{14}SiW_9$**) [24], $K_3Na_{17}H_{12}[(C_4H_6O_6)_6[Ni_4(OH)_3(A\text{-}\alpha\text{-}SiW_9O_{34})]_4]\cdot 96H_2O$ (**$Ni_{16}L_6(SiW_9)_4$**) [25], and $Na_{28}[\{Ni_4(OH)_3(VO_4)\}_4(B\text{-}PW_9O_{34})_4]\cdot 74H_2O$ (**$Ni_{16}(B\text{-}PW_9O_{34})_4$**) [26]. Recently, the coupled POM/semiconductor photocatalytic systems have been demonstrated to efficiently catalyze hydrogen evolution [27, 28], water oxidation[29], dehydrocoupling of thiophenols [30], the chemical transformation of organic [31–35], and selective hydrogenolysis of lignin β-O-4 models [36]. In this context, we are greatly inspired to explore the application of this coupled POM/semiconductor photocatalytic system in the oxidation valorization of 1-phenylethanol coupling with hydrogen evolution.

Herein, we employed the coupled **Ni_4P_2/ZIS/WO$_3$** photocatalytic system to catalyze oxidation valorization of 1-phenylethanol coupling with hydrogen evolution. Upon the optimized conditions, the conversion of 1-phenylethanol and the hydrogen production reached 99.9% and 202.4 μmol, respectively. Interestingly, the oxidation valorization product distribution of 1-phenylethanol depended on the catalytic system. The proposed photocatalytic mechanism was illustrated based on the results of several characterization techniques.

2 Experimental

2.1 Materials and instrumentation

Sodium tungstate ($Na_2WO_4\cdot 2H_2O$, 99%), sodium sulfate (Na_2SO_4, 99.5%), zinc chloride ($ZnCl_2$), indium chloride ($InCl_3$) and thioacetamide (TAA, CH_3CSNH_2) were purchased from Shanghai Aladdin. Acetonitrile (CH_3CN), ethanol (C_2H_5OH), and hydrochloric acid (HCl) were obtained from Beijing Chemical Plant. 1-Phenylethanol and acetophenone were purchased from Shanghai Macklin. All materials were used without further purification.

Fourier transform infrared (FT-IR) spectra were recorded on Bruker Tensor II with KBr pellets. High-resolution transmission electron microscopy (HR-TEM) images and element mapping images were recorded with an FEI Talos F200X. Scanning electron microscopy (SEM) were carried out on ZEISS supra55. X-ray photoelectron spectroscopy (XPS) data was collected using PHI QUANTERA-II SXM (ULVAC-PHI Co., Japan) with Al Kα. Electron paramagnetic resonance (EPR) spectra were recorded using A300-10/12 (Bruker Co., Germany). Ultraviolet–visible (UV–vis) spectra were collected on Techcomp UV 2600 spectrophotometer. Steady-state and time-resolved photoluminescence (PL) spectra were recorded by Edinburgh Instruments Spectrofluorometer FS5. Powder X-ray diffraction (PXRD) patterns were recorded using MiniFlex 600 diffractometer with a Cu-Kα X-ray radiation source. The electrochemical and photoelectrochemical (PEC) properties of the samples, such as, transient photocurrent and alternating current (AC) impedance, were measured at a CHI660E Electrochemical Workstation.

2.2 Preparation of WO_3 nanorods

WO_3 nanorods were prepared by a simple one-step hydrothermal method and the synthetic procedure was described as follows. $Na_2WO_4\cdot 2H_2O$ (40.0 g·L^{-1}) was dissolved in deionized (DI) water and then the pH was adjusted to 2.0 using hydrochloric acid (3.0 mol·L^{-1}). 3.0 g of oxalic acid and 3.0 g of anhydrous sodium sulfate were slowly added to the above solution under vigorous stirring. The resulting mixture was transferred to the 100 mL polytetrafluoroethylene (PTFE)-lined autoclave and kept at 180 °C for 24 h. After cooling to room temperature, the pale white WO_3 nanorods powder was obtained by washing three times with DI water and ethanol, drying overnight at 60 °C.

2.3 Preparation of $ZnIn_2S_4$ nanosheets

$ZnCl_2$, $InCl_3$ and CH_3CSNH_2 were added to the ethylene glycol solution containing 2 mL of DI water at the molar ratio of 1:2:4 under sonication and stirred vigorously for 30 min. The mixed solution was transferred to a PTFE-lined reaction vessel and maintained at 110 °C for 2 h. After cooling to room temperature, the yellow $ZnIn_2S_4$ nanosheets powder was collected by washing three times with DI water and ethanol, drying overnight at 60 °C.

2.4 Preparation of ZIS/WO_3 heterojunctions

The typical preparation of $ZnIn_2S_4$/WO_3 heterojunction, denoted as **ZIS/WO$_3$**-*x* where *x* represents the mole ratio of $ZnIn_2S_4$ and WO_3, was described as follows. The prepared WO_3 nanorods (0.5 mmol) were added to the 5 mL ethylene glycol solution containing $ZnCl_2$, $InCl_3$ and TAA with the molar ratio of 1:2:4 under vigorous stirring. The resulting mixture was then transferred to the PTFE-lined reaction vessel and kept at 110 °C for 2 h. After cooling to room temperature, the dark green powder **ZIS/WO$_3$** photocatalyst was collected by washing three times with DI water and ethanol, drying overnight at 60 °C. By varying the molar ratio of $ZnIn_2S_4$ and WO_3, a series of **ZIS/WO$_3$**-*x* (*x* = 2, 2.5, 3, 4) catalysts were obtained according to the above procedures.

2.5 Preparation of Na_6K_4-Ni_4P_2 and TBA-Ni_4P_2

Na_6K_4-**Ni_4P_2** was prepared according to our previous reported method [27]. The preparation of tetrabutylammonium (TBA^+) salt of **Ni_4P_2** (TBA-**Ni_4P_2**) was described as follows. 5 mg Na_6K_4-**Ni_4P_2** was dissolved in 40 mL H_2O, followed by adding 15 mL HAc/NaAc buffer solution (0.5 M, pH = 4.8) containing 5 g tetrabutylammonium bromide. A large amount of light-yellow precipitate appeared. Upon centrifugation, the resulting solid was re-dissolved in 5 mL of acetonitrile. The high-purity TBA-**Ni_4P_2** powder was collected after the addition of diethyl ether and centrifugation.

2.6 Photocatalytic tests

The photocatalytic oxidation of 1-phenylethanol coupled with hydrogen evolution experiments were performed in a cylindrical glass reactor under 300 W Xe lamp (PLS-SXE300D, 3 $W{\cdot}cm^{-2}$, Perfect Light) with a 400 nm cut-off filter. In a typical photocatalytic reaction, 10 mg of **ZIS/WO_3**-3 was dispersed in 6 mL of acetonitrile solution containing 50 mM 1-phenylethanol and 30 μM **Ni_4P_2** (Note: the TBA^+ salt of Ni_4P_2 was used in all photocatalytic studies unless otherwise noted). Upon degassing with Ar/CH_4 (volume ratio of 4/1), the reaction was illuminated by Xe lamp. After reaction, the gas product was detected by a gas chromatograph (GC-2014C) and the liquid product was analyzed by high-performance liquid chromatography (HPLC) (Shimadzu LC-20A). To obtain the high purity pinacol, the photocatalytic experiment was conducted under the optimized reaction conditions followed by the column chromatography. The GC and ^1H nuclear magnetic resonance (NMR) spectra of pinacol were shown in Fig. S1 in the Electronic Supplementary Material (ESM). The calibration curve was determined based on the HPLC spectra of different concentration of pinacol.

3 Results and discussion

The preparation of **ZIS/WO_3**-2.5 heterojunction was illustrated in Fig. 1(a) and the detailed procedures were described in the Experimental Section. Figure 1(b) showed the PXRD patterns of WO_3 nanorods, $ZnIn_2S_4$ nanosheets, and **ZIS/WO_3**-2.5 heterojunction. The well-matched diffraction peaks of WO_3 and $ZnIn_2S_4$ (JCPDS No. 33-1387, JCPDS No. 65-2023) [37, 38] indicated that the $ZnIn_2S_4$ nanosheets grew *in situ* on WO_3 nanorods. Transmission electron microscopy (TEM) images showed the nanorod-like structure of WO_3 (Fig. 1(c)) and nanoflower-like structure of $ZnIn_2S_4$ composed of two-dimensional ultra-thin nanosheets (Fig. 1(d)). Figure 1(e) and the HR-TEM image (Fig. 1(f)) clearly showed the lateral growth of $ZnIn_2S_4$ on the surface of WO_3 with the lattice fringe of 0.305 and 0.385 nm, respectively. The elemental mapping images indicated that the uniform distribution of the Zn, In, S, W, and O elements in **ZIS/WO_3**-2.5 heterojunction (Figs. 1(g)–1(l)).

The photocatalytic transformation of 1-phenylethanol was first conducted in acetonitrile solution over the **ZIS/WO_3**-2.5 S-scheme heterojunction (Fig. 2(a)). The conversion efficiency of **ZIS/WO_3**-2.5 heterojunction was significantly superior to that of individual $ZnIn_2S_4$ and WO_3 components (Fig. 2(b) and Table S1 in the ESM). The main oxidation products are acetophenone and C–C coupling product pinacol with the selectivity of 64.8% and 35.2%, respectively. Interestingly, the selectivity of acetophenone obviously increased to 93.8% when **Ni_4P_2** was added to the catalytic system (Fig. 2(c)). Moreover, the hydrogen production (183.1 μmol) of this coupled **Ni_4P_2**/**ZIS/WO_3**-2.5 catalytic system was superior to that of **ZIS/WO_3**-2.5 S-scheme heterojunction (155.6 μmol), indicating the essential role of **Ni_4P_2** in the production of hydrogen [39]. These tentative experimental results showed that the oxidative valorization of 1-phenylethanol depended on the catalytic conditions. 1-Phenylethanol tended to be converted to pinacol via C–C coupling reaction using **ZIS/WO_3**-2.5 S-scheme heterojunction as photocatalyst, while it was much easily oxidized to produce acetophenone in the presence of **Ni_4P_2** hydrogen evolution cocatalyst.

As shown in Figs. 2(b) and 2(c), the selectivity of pinacol over the coupled **Ni_4P_2**/**ZIS/WO_3**-2.5 catalytic system is inferior to that of

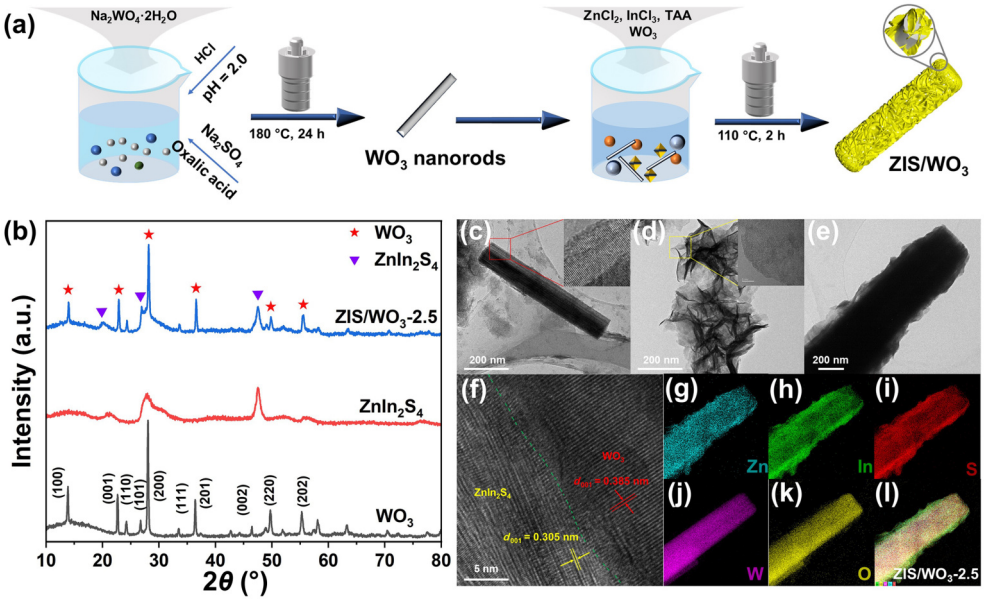

Figure 1 (a) The synthetic scheme of WO_3 nanorods and **ZIS/WO_3** heterojunction via hydrothermal method. (b) PXRD patterns of WO_3, $ZnIn_2S_4$, and **ZIS/WO_3**-2.5. TEM images of (c) WO_3 nanorods, (d) $ZnIn_2S_4$ nanosheets, and (e) **ZIS/WO_3**-2.5 heterojunction. (f) High-resolution TEM image of **ZIS/WO_3**-2.5 heterojunction. (g)–(l) Elemental mapping images of Zn, In, S, W, and O elements of **ZIS/WO_3**-2.5 heterojunction.

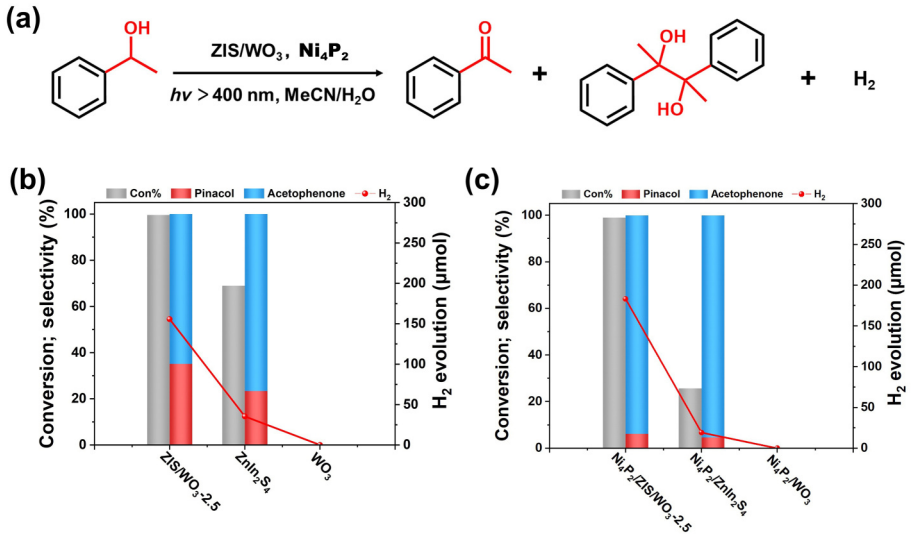

Figure 2 (a) The reaction equation of the photocatalytic oxidation of 1-phenylethanol. The photocatalytic results of various experiments over WO_3, $ZnIn_2S_4$, and **ZIS/WO$_3$**-2.5 S-scheme heterojunction in the (b) absence and (c) presence of **Ni$_4$P$_2$** cocatalyst.

ZIS/WO$_3$-2.5, which may be attributed to the prohibited acetophenone reduction. In this case, the presence of **Ni$_4$P$_2$** can compete with acetophenone for photogenerated electrons due to its excellent electron storage capacity, thereby prohibiting the acetophenone reduction process and the formation of pinacol. The participation of electrons is thus essential for the formation of pinacol. Besides, the yield of pinacol was closely related to the concentration of C-centered radicals in the reaction solution. Therefore, the concentration of substrates and the volume ratio of solvent (acetonitrile and water) were first investigated (Figs. 3(a) and 3(b) and Table S2 in the ESM). With the increment of the concentration of 1-phenylethanol (Fig. 3(a)), the selectivity of pinacol displayed the shape of volcano and reached the peak of 55.9% at the concentration of 50 mM. The influences of solvent on the photocatalytic activities were similar (Fig. 3(b)), because the certain amount of H_2O could enrich the C-centered radicals in acetonitrile to facilitate the C–C coupling generating the pinacol [40], while the excessive amount of H_2O would negatively affect the solubility of pinacol. Then, the amount of reduction photocatalyst $ZnIn_2S_4$ in **ZIS/WO$_3$** heterojunction was thus examined, the selectivity of pinacol reached 86.0% when the molar ratio of $ZnIn_2S_4$ and WO_3 was 3 (Fig. 3(c)). Therefore, the subsequent photocatalytic experiments toward the C–C coupling of 1-phenylethanol were conducted under the optimized reaction conditions (10 mg **ZIS/WO$_3$**-3, CH_3CN/H_2O (1:2), 50 mM 1-phenylethanol), unless otherwise noted. The time profiles (Fig. 3(d)) indicated that the C–C coupling reaction can be completely finished after 12 h photocatalysis with 99.9% conversion of 1-phenylethanol and 86.0% yield of pinacol.

To maximize the yield of oxidation product acetophenone, the usage of heterojunction semiconductor was first optimized (Fig. 3(e) and Table S3 in the ESM). With the increasing amount of **ZIS/WO$_3$**-2.5, the conversion of 1-phenylethanol, the selectivity of acetophenone and the hydrogen production first increased and reached the maximum at the using amount of 10 mg. The excessive amount of **ZIS/WO$_3$**-2.5 led to the decreased catalytic activities due to the light scattering effects. The influences of the concentration of **Ni$_4$P$_2$** on the photocatalytic activities were then investigated (Fig. 3(f) and Table S3 in the ESM). Despite of the unchanged conversion, both the selectivity of acetophenone and the hydrogen production gradually increased with the increasing concentration of **Ni$_4$P$_2$** and peaked (93.8%, 185.9 μmol) at the concentration of 50 μM. It is expected that further increasing the concentration of **Ni$_4$P$_2$** could improve the selectivity of acetophenone, but the optimized concentration of **Ni$_4$P$_2$** was herein selected as 50 μM in terms of economic benefits.

The photocatalytic stability in the two cases was examined for the five consecutive cycles (Figs. 3(g) and 3(h)). The selectivity of pinacol and acetophenone were almost unchanged after cycling experiments, respectively, indicating the good cycling stability of the catalytic system, which further confirmed by the PXRD patterns (Fig. S2 in the ESM), SEM (Fig. S3 in the ESM), and TEM (Fig. S4 in the ESM) images of **ZIS/WO$_3$** heterojunction. The conversion and the hydrogen production gradually decreased due to the photocatalyst loss during the post treatment. Additionally, the decline amplitude of the conversion in Fig. 3(h) was more obvious than that in Fig. 3(g), which could be resulted from the greater loss of **ZIS/WO$_3$** photocatalyst in acetonitrile as it disperses more readily compared to the mixed solution of acetonitrile and water. The stability of **Ni$_4$P$_2$** was also evaluated. The FT-IR spectrum of the isolated **Ni$_4$P$_2$** by $[Ru(bpy)_3]Cl_2{\cdot}6H_2O$ after reaction was shown in Fig. 3(i). The well matched characteristic vibration peaks of P–O, W=O and W–O–W confirmed the good catalytic stability of **Ni$_4$P$_2$** [41].

To clarify the transfer behavior of the photogenerated charge carriers, a series of characterization techniques were employed for WO_3 nanorods, $ZnIn_2S_4$ nanosheets, and **ZIS/WO$_3$** heterojunction. The absorption intensity of **ZIS/WO$_3$** in the UV–vis spectra (Fig. 4(a)) was obviously improved, indicating the enhanced visible light absorption of $ZnIn_2S_4$ nanosheets due to the formation of **ZIS/WO$_3$** heterojunction. The calculated band gaps of WO_3 and $ZnIn_2S_4$ according to Kubelka-Munk theory were 3.04 and 2.44 eV, respectively. The positive slopes of the Mott–Schottky curves identified the n-type semiconductor properties of both WO_3 nanorods and $ZnIn_2S_4$ nanosheets (Figs. 4(b) and 4(c)). The measured flat-band potentials of WO_3 nanorods and $ZnIn_2S_4$ nanosheets were −0.41 and −1.11 V vs. Ag/AgCl, respectively, which is consistent with the previous reports [42]. The CB

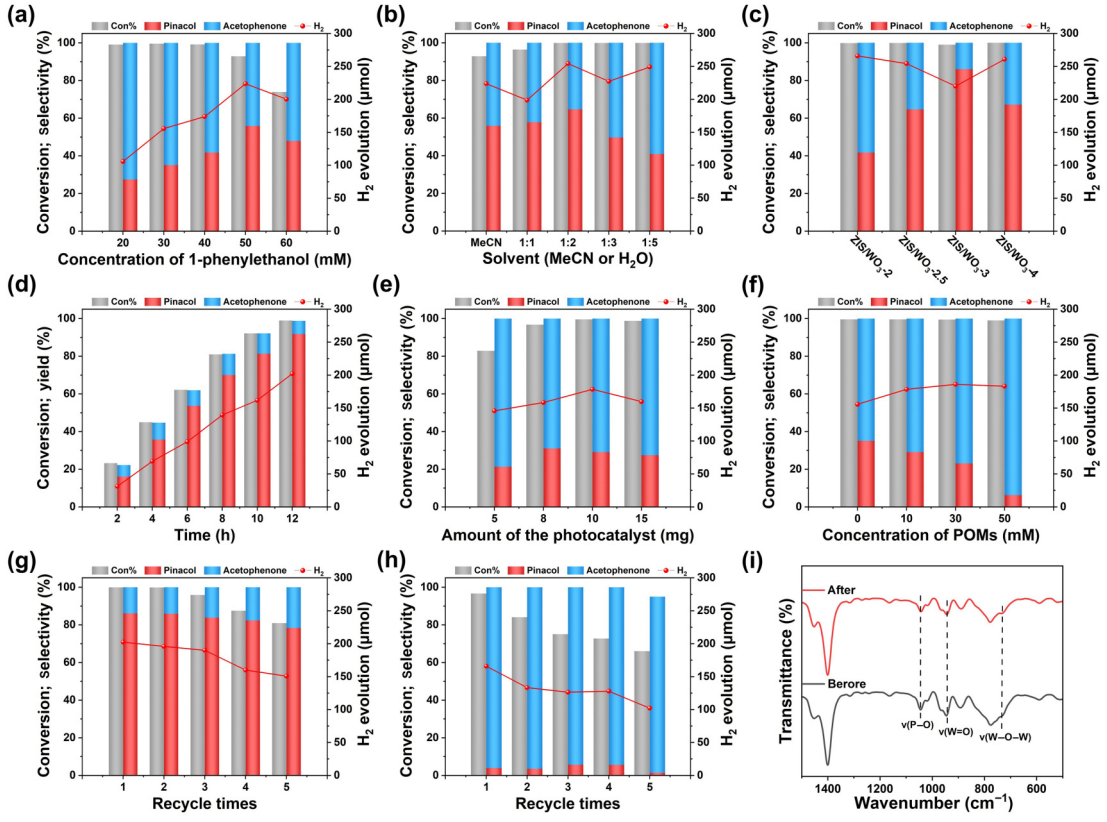

Figure 3 The photocatalytic activities as functions of (a) the concentration of 1-phenylethanol, (b) the volume ratio of acetonitrile and water, and (c) the molar ratio of $ZnIn_2S_4$ and WO_3. (d) The time profiles of the C–C coupling of 1-phenylethanol. The photocatalytic activities as functions of (e) the using amount of **ZIS/WO$_3$**-2.5 heterojunction and (f) the concentration of **Ni$_4$P$_2$**. The photocatalytic recycling tests of (g) the oxidation and (h) C–C coupling of 1-phenylethanol. (i) FT-IR spectra of **Ni$_4$P$_2$** before and after photocatalysis.

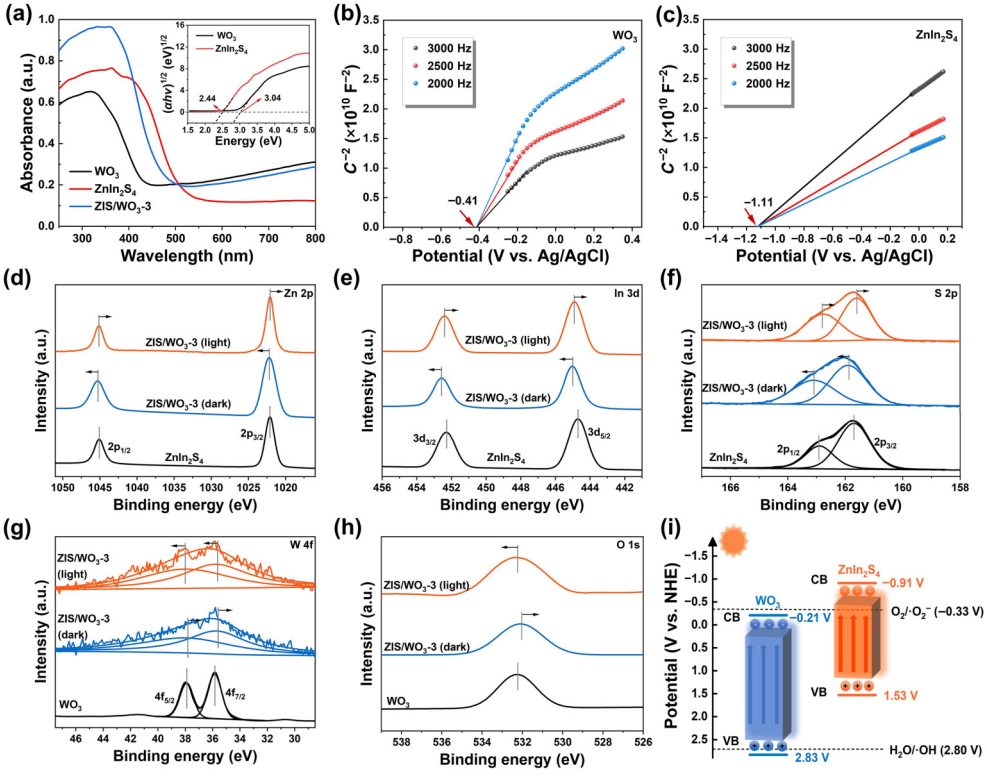

Figure 4 (a) UV–vis spectra of WO_3, $ZnIn_2S_4$, and **ZIS/WO$_3$**-3. The inset is the Tauc plots of WO_3 and $ZnIn_2S_4$. Mott–Schottky (M–S) plots of (b) WO_3 and (c) $ZnIn_2S_4$. High-resolution (d) Zn 2p, (e) In 3d, (f) S 2p, (g) W 4f and (h) O 1s XPS spectra of the $ZnIn_2S_4$ and **ZIS/WO$_3$**-3 heterojunction in dark and under illumination. (i) The band structures of WO_3 and $ZnIn_2S_4$.

potentials of WO_3 nanorods and $ZnIn_2S_4$ nanosheets were determined to be −0.21 and −0.91 V vs. NHE (pH = 6) according to the formula of $E_{NHE} = E_{Ag/AgCl} + 0.20$ V [43]. The calculated VB potentials of WO_3 nanorods and $ZnIn_2S_4$ nanosheets and the energy band diagram were plotted in Fig. 4(i). The oxidation potential of 1-phenylethanol (1.41 V vs. NHE), determined by electrochemical cyclic voltammetry (CV) curve (Fig. S5 in the ESM), was lower than the VB potential of $ZnIn_2S_4$ nanosheets, confirming its feasibility to oxidizing 1-phenylethanol.

The survey XPS spectrum confirmed the existence of Zn, In, S, W, and O elements in **ZIS/WO$_3$**-3 heterojunction (Fig. S6 in the ESM). Those most prominent signals observed at 1022.1, 445.1, and 161.7 eV are assigned to Zn $2p_{3/2}$, In $3d_{5/2}$, and S $2p_{3/2}$ peaks, respectively (Figs. 4(d)–4(f)). The spin-orbit splitting values for each element is 23.0, 7.5, and 1.2 eV for Zn 2p, In 3d, and S 2p spectra, respectively. Moreover, the intensity ratios of two spin-orbit separation peaks in each spectrum are 1:2 (Zn 2p), 2:3 (In 3d), and 1:2 (S 2p), which agree well with the Zn^{2+}, In^{3+}, and S^{2-} chemical states in $ZnIn_2S_4$. Upon the formation of heterojunction, the binding energies of Zn, In, and S shifted to the high binding energies while that of W and O shifted to the low binding energy (Figs. 4(g) and 4(h)), indicating the transfer of electrons from $ZnIn_2S_4$ to WO_3. However, the binding energies of these elements shifted in the opposite direction after the photocatalysis, indicating the return of electrons into $ZnIn_2S_4$ during the photocatalytic process. The change in the direction of electron transfer before and after photocatalysis is the typical characters of S-scheme heterojunction.

To further confirm the S-scheme heterojunction of **ZIS/WO$_3$**-3, we conducted the following control experiments using the photooxidation of 5-hydroxymethylfurfural (HMF) as the model reaction (Tables S4 and S5 in the ESM). It is well known that the formation of $\cdot O_2^-$ species can efficiently facilitate the photooxidation of HMF under O_2 atmosphere if the CB of photocatalyst is well matched with the reduction potential of O_2 [44]. As shown in Table S4 in the ESM, the conversion of HMF over WO_3 nanorods was inferior to that of $ZnIn_2S_4$ nanosheets and **ZIS/WO$_3$**-3 heterojunction under O_2 atmosphere, because the $\cdot O_2^-$ species cannot be produced due to the insufficient reduction capacity of WO_3 nanorods while it can be easily formed on the $ZnIn_2S_4$ nanosheets and **ZIS/WO$_3$**-3 heterojunction surface owing to the strong reduction ability (Fig. 4(i)). Under Ar atmosphere, the conversion of HMF significantly decreased over both $ZnIn_2S_4$ nanosheets and **ZIS/WO$_3$**-3 heterojunction, further identifying the crucial role of $\cdot O_2^-$ species during the photocatalysis. The variation in the conversion of HMF was likewise similar over three semiconductors under the presence of H_2O due to the promoting effect of ·OH species [45]. The ·OH species cannot be produced on $ZnIn_2S_4$ nanosheets due to its weak oxidation ability whereas WO_3 nanorods and **ZIS/WO$_3$**-3 heterojunction have sufficient oxidation capacity to oxidize H_2O producing ·OH (Fig. 4(i)) leading to higher conversion of HMF (Table S5 in the ESM).

The advantages in the photogenerated charge carriers transfer of **ZIS/WO$_3$**-3 S-scheme heterojunction was also examined by transient photocurrent tests, electrochemical impedance, and PL emission techniques (Fig. 5). As shown in Fig. 5(a), the significantly enhanced photocurrent of **ZIS/WO$_3$**-3 confirmed the effective separation efficiency of the photogenerated charge carriers in S-scheme heterojunction. The smaller arc radius in the electrochemical impedance spectrum indicated lower electron transfer resistance for the **ZIS/WO$_3$**-3 S-scheme heterojunction (Fig. 5(b)) [46], which is consistent with the results of photocurrent tests. The kinetics of photogenerated charge transfer were also evaluated using steady-state and time-resolved PL emission spectra (Figs. 5(c) and 5(d)). Upon 365 nm laser irradiation, an obvious strong PL signal (370–720 nm) for **ZIS/WO$_3$**-3 S-scheme heterojunction was remarkably quenched by the addition of the substrate and **Ni_4P_2**, suggesting the efficient transfer of

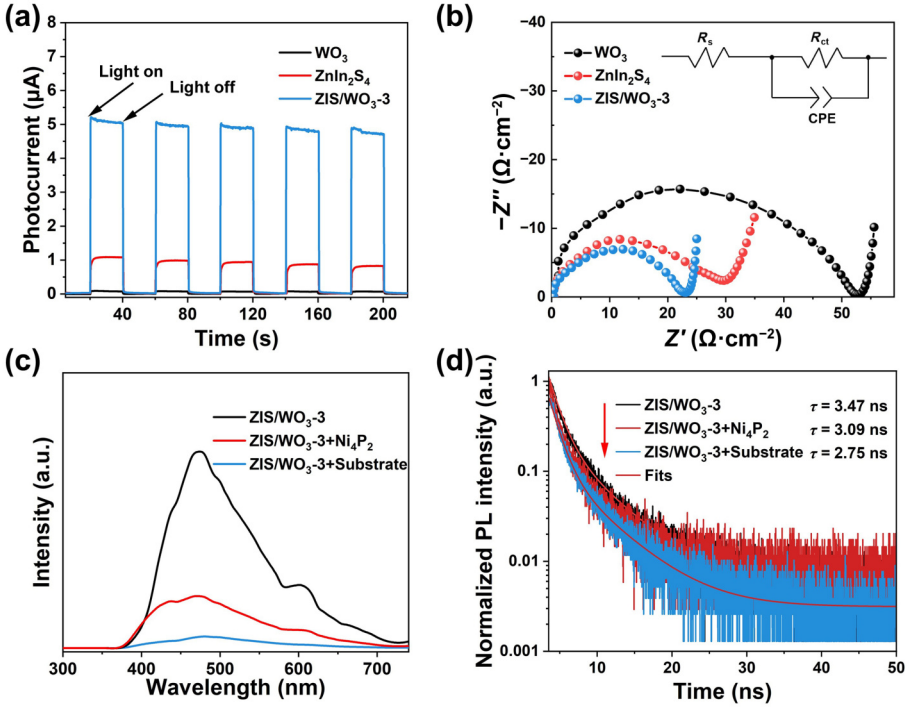

Figure 5 (a) The photocurrent tests and (b) EIS Nyquist plots of WO_3, $ZnIn_2S_4$, and **ZIS/WO$_3$**-3. (c) Steady-state and (d) time-resolved photoluminescence spectra of **ZIS/WO$_3$**-3 and the addition of **Ni_4P_2** and substrate.

photoinduced electrons from **ZIS/WO$_3$**-3 to 1-phenylphenone or **Ni$_4$P$_2$**, respectively, which further confirmed by the decreased PL decay lifetimes (Fig. 5(d) and Table S6 in the ESM).

Various control experiments were conducted to clarify the photocatalytic reaction mechanism. No product was observed in dark indicating the necessity of light irradiation for photocatalysis (Fig. 6(a)). Adding triethanolamine (TEOA) as the hole scavenger to the catalytic system significantly decreased the photocatalytic activities, suggesting the crucial role of the photogenerated holes in the effective photocatalysis. In the presence of isopropanol (IPA), the almost unchanged photocatalytic activities indicated that the ·OH was not the active species for the photooxidation of 1-phenylethanol. The introduction of 5,5-dimethyl-1-pyrroline N-oxide (DMPO) as the carbon free radical scavenger declined the conversion of 1-phenylethanol and the yield of pinacol, but the yield of acetophenone enhanced, which implied that the carbon radical was essential for the production of pinacol but not for the formation of acetophenone. The formation of C-centered radicals was confirmed by the electron paramagnetic resonance (EPR) signals (Fig. 6(b)). No EPR signals of C-centered radicals were detected in dark, whereas six characteristic signal peaks with coupling constants of a_N = 16.1 and a_H = 22.7 were observed after light irradiation for 10 min. Additionally, the addition of $Na_2S_2O_8$ as electron scavenger had little effects on the conversion of 1-phenylethanol, but the main product changed into acetophenone from pinacol, which identified the necessity of the photogenerated electrons towards the production of pinacol. The absence of pinacol after the addition of **PW$_{12}$** further confirmed the crucial role of photogenerated electrons in the formation of pinacol, because **PW$_{12}$** acting as electron-storing mediator/sponge resulted in the formation of deep blue color (known as "heteropoly blue") inhibited the photocatalysis (Fig. S7 in the ESM). It is thus inferred that the production of pinacol resulted from the reduction of acetophenone. The reduction potential of acetophenone (−0.41 V vs. NHE), determined by CV curve in Fig. S8 in the ESM, was lower than the CB of $ZnIn_2S_4$, which confirmed the feasibility of the reduction of acetophenone by the photogenerated electrons.

Based on the above-mentioned analyses, the photocatalytic reaction mechanism was proposed as follows (Fig. 6(c)). Under visible light irradiation, the photogenerated electrons and holes accumulated on the CB of $ZnIn_2S_4$ and the VB of WO_3, respectively, according to the electron transfer route of S-scheme heterojunction driven by the built-in electric field [47]. The photogenerated holes oxidized 1-phenylethanol generating the acetophenone, which was rapidly reduced by the powerful accumulated electrons on CB of $ZnIn_2S_4$ forming C_α-centered radical, promoting the C–C coupling reaction and finally produced pinacol. If **Ni$_4$P$_2$** was added to the catalyst system, the photogenerated electrons were then swiftly transferred to **Ni$_4$P$_2$**, leading to the inhibition of acetophenone reduction, meanwhile the hydrogen species originated from 1-phenylethanol captured by **Ni$_4$P$_2$** and then reduced by the photogenerated electrons to produce H_2.

4 Conclusion

In conclusion, the coupled catalytic system comprising **ZIS/WO$_3$**-3 S-scheme heterojunction and **Ni$_4$P$_2$** has been constructed and further utilized to catalyze the photocatalytic oxidation valorization

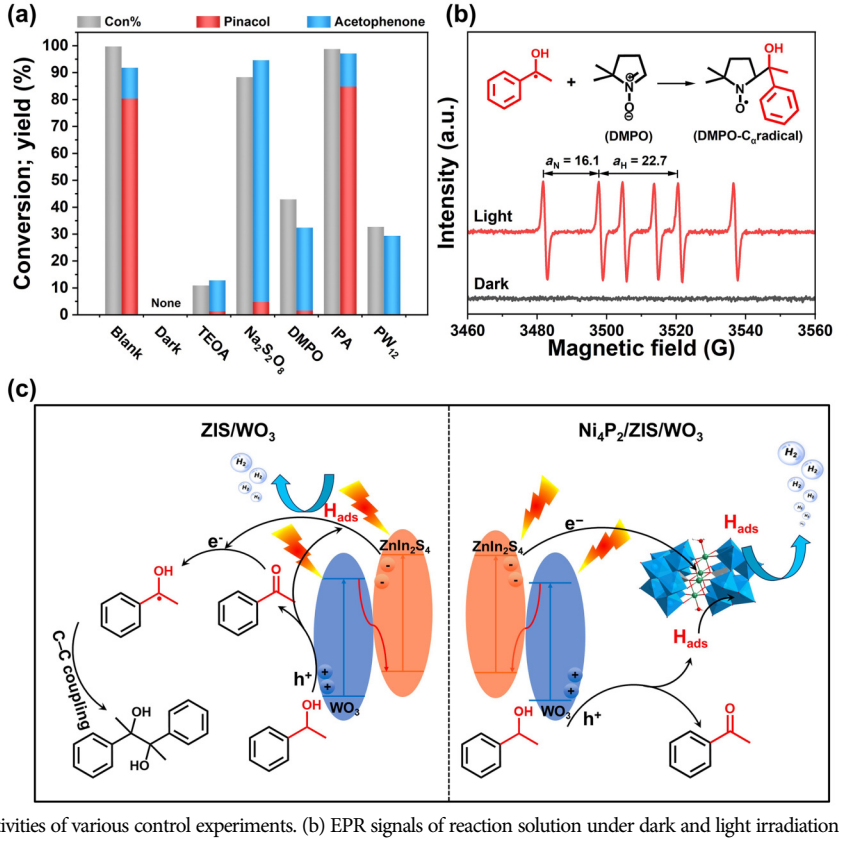

Figure 6 (a) Photocatalytic activities of various control experiments. (b) EPR signals of reaction solution under dark and light irradiation for 10 min (λ > 400 nm) in the presence of **ZIS/WO$_3$**-3. (c) The proposed mechanism of photocatalytic oxidation of 1-phenylethanol coupled with H_2 production based on **ZIS/WO$_3$**-3 S-scheme heterojunction.

of 1-phenylethanol coupling with hydrogen evolution. The photocatalytic oxidation reaction can be finished after 12 h photocatalysis based on **ZIS/WO_3**-3 S-scheme heterojunction, leading to the 99.9% conversion of 1-phenylethanol with the 86.0% selectivity of pinacol and 202.4 μmol H_2, respectively. Interestingly, 1-phenylethanol can be highly selectively converted to acetophenone (99.1% selectivity) accompanied by hydrogen production (183.1 μmol) in the addition **Ni_4P_2** to the catalytic system. The catalytic system showed good photocatalytic recycling stability for both the two reaction conditions. A series of characterization results indicated that **ZIS/WO_3**-3 S-scheme heterojunction promoted the efficient separation and migration and maximized the redox capacity of the photogenerated electrons and holes, resulting in the excellent photocatalytic performances. Comprehensive experiments and characterizations results revealed that 1-phenylethanol would be preferentially oxidized into acetophenone by photogenerated holes on VB of WO_3, which can be swiftly reduced by powerful accumulated electrons on CB of $ZnIn_2S_4$ forming C_α-centered radicals over **ZIS/WO_3**-3 S-scheme heterojunction, and finally produced pinacol via the coupling of two C_α-centered radical. if **Ni_4P_2** was added to the catalytic system, the photogenerated electrons were rapidly transferred to **Ni_4P_2**, resulting in the dominant formation of acetophenone due to the inhibition of its reduction by **Ni_4P_2**. Our current work provides valuable insights into the sustainable development of the efficient valorization of biomass and hydrogen production.

Electronic Supplementary Material: Supplementary material (Experimental, Figs. S1–S8, and Tables S1–S6) is available in the online version of this article at https://doi.org/10.26599/NR.2025.94907303.

Data availability

All data needed to support the conclusions in the paper are presented in the manuscript and the Electronic Supplementary Material. Additional data related to this paper may be requested from the corresponding author upon request.

Acknowledgements

We gratefully acknowledge the financial support from the National Natural Science Foundation of China (Nos. 22008012 and 22471019), the Hebei Natural Science Foundation (No. B2024105003), Development and Reform Commission Project of Jilin Province (No. 2024C020-2), the Recruitment Program of Global Experts (Young Talents) and BIT Excellent Young Scholars Research Fund. The instrumental support from the Analysis and Testing Center of Beijing Institute of Technology is also highly appreciated.

Declaration of competing interest

All the contributing authors report no conflict of interests in this work.

Author contribution statement

J. X. Y.: Data curation, formal analysis, investigation, writing – original draft. Y. K. L. and Y. Q.: Validation, visualization. Z. H. D., Y. Y. D., and H. J. L.: Project administration, funding acquisition, supervision, validation, writing – review & editing.

Use of AI statement

None.

References

[1] Wakerley, D. W.; Kuehnel, M. F.; Orchard, K. L.; Ly, K. H.; Rosser, T. E.; Reisner, E. Solar-driven reforming of lignocellulose to H_2 with a CdS/CdO_x photocatalyst. *Nat. Energy* **2017**, *2*, 17021.

[2] Wang, E. Y.; Mahmood, A.; Chen, S. G.; Sun, W. H.; Muhmood, T.; Yang, X. F.; Chen, Z. P. Solar-driven photocatalytic reforming of lignocellulose into H_2 and value-added biochemicals. *ACS Catal.* **2022**, *12*, 11206–11215.

[3] Fujishima, A.; Honda, K. Electrochemical photolysis of water at a semiconductor electrode. *Nature* **1972**, *238*, 37–38.

[4] Gu, M. L.; Yang, Y.; Zhang, L. Y.; Zhu, B. C.; Liang, G. J.; Yu, J. G. Efficient sacrificial-agent-free solar H_2O_2 production over all-inorganic S-scheme composites. *Appl. Catal. B: Environ.* **2023**, *324*, 122227.

[5] Xu, Q. L.; Zhang, L. Y.; Cheng, B.; Fan, J. J.; Yu, J. G. S-scheme heterojunction photocatalyst. *Chem* **2020**, *6*, 1543–1559.

[6] Zhu, B. C.; Sun, J.; Zhao, Y. Y.; Zhang, L. Y.; Yu, J. G. Construction of 2D S-scheme heterojunction photocatalyst. *Adv. Mater.* **2024**, *36*, 2310600.

[7] Fu, J. W.; Xu, Q. L.; Low, J. X.; Jiang, C. J.; Yu, J. G. Ultrathin 2D/2D WO_3/g-C_3N_4 step-scheme H_2-production photocatalyst. *Appl. Catal. B: Environ.* **2019**, *243*, 556–565.

[8] Wang, W. L.; Zhao, W. L.; Zhang, H. C.; Dou, X. C.; Shi, H. F. 2D/2D step-scheme α-Fe_2O_3/Bi_2WO_6 photocatalyst with efficient charge transfer for enhanced photo-Fenton catalytic activity. *Chin. J. Catal.* **2021**, *42*, 97–106.

[9] Wang, L. B.; Cheng, B.; Zhang, L. Y.; Yu, J. G. *In situ* irradiated XPS investigation on S-scheme TiO_2@$ZnIn_2S_4$ photocatalyst for efficient photocatalytic CO_2 reduction. *Small* **2021**, *17*, 2103447.

[10] Wang, Z. L.; Cheng, B.; Zhang, L. Y.; Yu, J. G.; Tan, H. Y. BiOBr/NiO S-scheme heterojunction photocatalyst for CO_2 photoreduction. *Sol. RRL* **2022**, *6*, 2100587.

[11] Li, T.; Tsubaki, N.; Jin, Z. L. S-scheme heterojunction in photocatalytic hydrogen production. *J. Mater. Sci. Technol.* **2024**, *169*, 82–104.

[12] Wang, L. X.; Zhu, B. C.; Zhang, J. J.; Ghasemi, J. B.; Mousavi, M.; Yu, J. G. S-scheme heterojunction photocatalysts for CO_2 reduction. *Matter* **2022**, *5*, 4187–4211.

[13] Han, X. X.; Lu, B. J.; Huang, X.; Liu, C.; Chen, S. X.; Chen, J. W.; Zeng, Z. L.; Deng, S. G.; Wang, J. Novel p- and n-type S-scheme heterojunction photocatalyst for boosted CO_2 photoreduction activity. *Appl. Catal. B: Environ.* **2022**, *316*, 121587.

[14] Wang, L. X.; Sun, J.; Cheng, B.; He, R. A.; Yu, J. G. S-scheme heterojunction photocatalysts for H_2O_2 production. *J. Phys. Chem. Lett.* **2023**, *14*, 4803–4814.

[15] Zhang, Y. M.; Jin, Z. Z.; Liu, D.; Tan, Z. T.; Mamba, B. B.; Kuvarega, A. T.; Gui, J. Z. S-scheme Bi_2S_3/CdS nanorod heterojunction photocatalysts with improved carrier separation and redox capacity for pollutant removal. *ACS Appl. Nano Mater.* **2022**, *5*, 5448–5458.

[16] Bariki, R.; Das, K.; Pradhan, S. K.; Prusti, B.; Mishra, B. G. MOF-derived hollow tubular In_2O_3/$M^{II}In_2S_4$ (M^{II}: Ca, Mn, and Zn) heterostructures: Synergetic charge-transfer mechanism and excellent photocatalytic performance to boost activation of small atmospheric molecules. *ACS Appl. Energy Mater.* **2022**, *5*, 11002–11017.

[17] Cheng, C.; Zhu, B. C.; Cheng, B.; Macyk, W.; Wang, L. X.; Yu, J. G. Catalytic conversion of styrene to benzaldehyde over S-scheme photocatalysts by singlet oxygen. *ACS Catal.* **2023**, *13*, 459–468.

[18] Fan, Y. S.; Xi, X. L.; Liu, Y. S.; Nie, Z. R.; Zhao, L. Y.; Zhang, Q. H. Regulation of morphology and visible light-driven photocatalysis of WO_3 nanostructures by changing pH. *Rare Met.* **2021**, *40*, 1738–1745.

[19] Zhang, M.; Li, H. J.; Zhang, J. H.; Lv, H. J.; Yang, G. Y. Research

advances of light-driven hydrogen evolution using polyoxometalate-based catalysts. *Chin. J. Catal.* **2021**, *42*, 855–871.

[20] Lv, H. J.; Guo, W. W.; Wu, K. F.; Chen, Z. Y.; Bacsa, J.; Musaev, D. G.; Geletii, Y. V.; Lauinger, S. M.; Lian, T. Q.; Hill, C. L. A noble-metal-free, tetra-nickel polyoxotungstate catalyst for efficient photocatalytic hydrogen evolution. *J. Am. Chem. Soc.* **2014**, *136*, 14015–14018.

[21] Lv, H. J.; Chi, Y. N.; van Leusen, J.; Kögerler, P.; Chen, Z. Y.; Bacsa, J.; Geletii, Y. V.; Guo, W. W.; Lian, T. Q.; Hill, C. L. $[\{Ni_4(OH)_3AsO_4\}_4(B\text{-}\alpha\text{-}PW_9O_{34})_4]^{28-}$: A new polyoxometalate structural family with catalytic hydrogen evolution activity. *Chem.—Eur. J.* **2015**, *21*, 17363–17370.

[22] von Allmen, K.; Moré, R.; Müller, R.; Soriano-López, J.; Linden, A.; Patzke, G. R. Nickel-containing keggin-type polyoxometalates as hydrogen evolution catalysts: Photochemical structure-activity relationships. *ChemPlusChem* **2015**, *80*, 1389–1398.

[23] Wang, Y. Q.; Xin, X.; Feng, Y. Q.; Chi, M. Z.; Wang, R. J.; Liu, T. F.; Lv, H. J. Structurally-new hexadecanuclear Ni-containing silicotungstate with catalytic hydrogen generation activity. *Molecules* **2023**, *28*, 2017.

[24] Paille, G.; Boulmier, A.; Bensaid, A.; Ha-Thi, M. H.; Tran, T. T.; Pino, T.; Marrot, J.; Rivière, E.; Hendon, C. H.; Oms, O. et al. An unprecedented $\{Ni_{14}SiW_9\}$ hybrid polyoxometalate with high photocatalytic hydrogen evolution activity. *Chem. Commun.* **2019**, *55*, 4166–4169.

[25] Li, J.; Feng, Y. Q.; Fu, F. Y.; Xin, X.; Yang, G. Y.; Lv, H. J. Polyoxometalate-organic cage with $\{Ni_4SiW_9\}$ node for photocatalytic hydrogen evolution. *Chin. Chem. Lett.* **2024**, *35*, 108736.

[26] Han, X. B.; Qin, C.; Wang, X. L.; Tan, Y. Z.; Zhao, X. J.; Wang, E. B. Bio-inspired assembly of cubane-adjustable polyoxometalate-based high-nuclear nickel clusters for visible light-driven hydrogen evolution. *Appl. Catal. B: Environ.* **2017**, *211*, 349–356.

[27] Zhang, M.; Xin, X.; Feng, Y. Q.; Zhang, J. H.; Lv, H. J.; Yang, G. Y. Coupling Ni-substituted polyoxometalate catalysts with water-soluble CdSe quantum dots for ultraefficient photogeneration of hydrogen under visible light. *Appl. Catal. B: Environ.* **2022**, *303*, 120893.

[28] Zhang, J. H.; Zhang, M.; Dong, Y. Y.; Bai, C. C.; Feng, Y. Q.; Jiao, L.; Lv, H. J. CdTe/CdSe-sensitized photocathode coupling with Ni-substituted polyoxometalate catalyst for photoelectrochemical generation of hydrogen. *Nano Res.* **2022**, *15*, 1347–1354.

[29] Paille, G.; Gomez-Mingot, M.; Roch-Marchal, C.; Lassalle-Kaiser, B.; Mialane, P.; Fontecave, M.; Mellot-Draznieks, C.; Dolbecq, A. A fully noble metal-free photosystem based on cobalt-polyoxometalates immobilized in a porphyrinic metal-organic framework for water oxidation. *J. Am. Chem. Soc.* **2018**, *140*, 3613–3618.

[30] Ren, M. Z.; Liu, T. F.; Dong, Y. Y.; Li, Z.; Yang, J. X.; Diao, Z. H.; Lv, H. J.; Yang, G. Y. Near-unity photocatalytic dehydrocoupling of thiophenols into disulfides and hydrogen using coupled CdS Nanorods and Ni-containing polyoxometalate. *Chin. J. Catal.* **2024**, *61*, 312–321.

[31] Suzuki, K.; Mizuno, N.; Yamaguchi, K. Polyoxometalate photocatalysis for liquid-phase selective organic functional group transformations. *ACS Catal.* **2018**, *8*, 10809–10825.

[32] Wang, Q.; Du, J.; Ma, Y. Y.; Yin, X. Y.; Tian, Z. Y.; Han, Z. G. Noble-metal-free 3D hierarchical Ni–WC heterostructure with enhanced interfacial charge transfer for efficient electrocatalytic hydrodechlorination. *Chem. Eng. J.* **2023**, *451*, 139107.

[33] Wang, Q.; Liu, Q.; Ma, Y. Y.; Bi, H. X.; Du, J.; Han, Z. G. A photocatalyst with an enhanced Schottky effect and an efficient electron-transfer channel fabricated by assembling Ni–WC heterojunction nanoparticles on g-C_3N_4 for highly efficient removal of chlorophenols. *Inorg. Chem. Front.* **2024**, *11*, 1238–1251.

[34] Wang, Q. W.; Wang, J. X.; Zhang, D.; Chen, Y. N.; Wang, J.; Wang, X. H. Fabrication of macroporous POMs/biochar materials for fast degradation of phthalic acid esters through adsorption coupled with aerobic oxidation. *Polyoxometalates* **2024**, *3*, 9140064.

[35] Wang, Y.; Liu, Q.; Ma, Y. Y.; Liu, Z. X.; Zhang, Y. N.; Wang, Y. S.; Du, J.; Han, Z. G. Polyoxometalate-embedded copper-organic network as dual-site synergetic catalyst for the selective oxidation of benzylic C–H bond. *Mol. Catal.* **2024**, *569*, 114579.

[36] Zhang, M.; Li, Z.; Feng, Y. Q.; Xin, X.; Yang, G. Y.; Lv, H. J. Highly selective hydrogenolysis of lignin β-O-4 models by a coupled polyoxometalate/CdS photocatalytic system. *Green Chem.* **2023**, *25*, 10091–10100.

[37] Weng, B.; Wu, J.; Zhang, N.; Xu, Y. J. Observing the role of graphene in boosting the two-electron reduction of oxygen in graphene-WO_3 nanorod photocatalysts. *Langmuir* **2014**, *30*, 5574–5584.

[38] Wang, J.; Sun, S. J.; Zhou, R.; Li, Y. Z.; He, Z. T.; Ding, H.; Chen, D. M.; Ao, W. H. A review: Synthesis, modification and photocatalytic applications of $ZnIn_2S_4$. *J. Mater. Sci. Technol.* **2021**, *78*, 1–19.

[39] Jiao, L.; Dong, Y. Y.; Xin, X.; Qin, L.; Lv, H. J. Facile integration of Ni-substituted polyoxometalate catalysts into mesoporous light-responsive metal-organic framework for effective photogeneration of hydrogen. *Appl. Catal. B: Environ.* **2021**, *291*, 120091.

[40] Han, G. Q.; Liu, X. W.; Cao, Z.; Sun, Y. J. Photocatalytic pinacol C–C coupling and jet fuel precursor production on $ZnIn_2S_4$ nanosheets. *ACS Catal.* **2020**, *10*, 9346–9355.

[41] Dong, Y. Y.; Feng, Y. Q.; Li, Z.; Zhou, H.; Lv, H. J.; Yang, G. Y. $CsPbBr_3$/polyoxometalate composites for selective photocatalytic oxidation of benzyl alcohol. *ACS Catal.* **2023**, *13*, 14346–14355.

[42] Zhao, M. Y.; Liu, S.; Chen, D. M.; Zhang, S. S.; Carabineiro, S. A. C.; Lv, K. L. A novel S-scheme 3D $ZnIn_2S_4/WO_3$ heterostructure for improved hydrogen production under visible light irradiation. *Chin. J. Catal.* **2022**, *43*, 2615–2624.

[43] He, B. W.; Xiao, P.; Wan, S. J.; Zhang, J. J.; Chen, T.; Zhang, L. Y.; Yu, J. G. Rapid charge transfer endowed by interfacial Ni–O bonding in S-scheme heterojunction for efficient photocatalytic H_2 and imine production. *Angew. Chem., Int. Ed.* **2023**, *62*, e202313172.

[44] Zhang, M.; Li, Z.; Xin, X.; Zhang, J. H.; Feng, Y. Q.; Lv, H. J. Selective valorization of 5-hydroxymethylfurfural to 2, 5-diformylfuran using atmospheric O_2 and $MAPbBr_3$ perovskite under visible light. *ACS Catal.* **2020**, *10*, 14793–14800.

[45] Xue, W. H.; Ye, J.; Zhu, Z.; Kumar, R.; Zhao, J. Harnessing trace water for enhanced photocatalytic oxidation of biomass-derived alcohols to aldehydes. *Energy Environ. Sci.* **2025**, *18*, 214–226.

[46] Liu, F.; Fu, Y. W.; Lu, K. J.; Wang, S. J.; Wang, B.; Huang, J.; Yan, X. L.; Zheng, Y. Q.; Guo, L. J.; Liu, M. C. Solar reforming lignocellulose into H_2 over pH-triggered hydroxyl-functionalized chalcogenide nanotwins. *ACS Catal.* **2023**, *13*, 15591–15602.

[47] Ma, F. H.; Wang, S. H.; Han, L. Y.; Guo, Y. H.; Wang, Z. Y.; Wang, P.; Liu, Y. Y.; Cheng, H. F.; Dai, Y.; Zheng, Z. K. et al. Targeted regulation of the electronic states of nickel toward the efficient electrosynthesis of benzonitrile and hydrogen production. *ACS Appl. Mater. Interfaces* **2021**, *13*, 56140–56150.